ResearchGate

See discussions, stats, and author profiles for this publication at: https://www.researchgate.net/publication/322621003

A Facile Space-Confined Solid-Phase Sulfurization Strategy for Growth of High-Quality Ultrathin Molybdenum Disulfide Single Crystals

Article *in* Nano Letters · January 2018

DOI: 10.1021/acs.nanolett.7b05473

CITATIONS
36

READS
403

16 authors, including:

Dawei Li
Dalian University of Technology
67 PUBLICATIONS **1,070** CITATIONS

SEE PROFILE

Zhiyong Xiao
University of Nebraska at Lincoln
25 PUBLICATIONS **381** CITATIONS

SEE PROFILE

Sai Mu
University of South Carolina
73 PUBLICATIONS **1,159** CITATIONS

SEE PROFILE

Fei Wang
University of Nebraska at Lincoln
42 PUBLICATIONS **516** CITATIONS

SEE PROFILE

Some of the authors of this publication are also working on these related projects:

Project Laser-induced breakdown spectroscopy View project

Project Organic Ferroelectric Materials View project

All content following this page was uploaded by Dawei Li on 19 August 2019.

The user has requested enhancement of the downloaded file.

NANO LETTERS

Letter

Cite This: *Nano Lett.* 2018, 18, 2021−2032

pubs.acs.org/NanoLett

A Facile Space-Confined Solid-Phase Sulfurization Strategy for Growth of High-Quality Ultrathin Molybdenum Disulfide Single Crystals

Dawei Li,[*,†] Zhiyong Xiao,[‡,§] Sai Mu,[∥] Fei Wang,[⊥] Ying Liu,[†] Jingfeng Song,[‡,§] Xi Huang,[†] Lijia Jiang,[†] Jun Xiao,[†] Lei Liu,[†] Stephen Ducharme,[‡,§] Bai Cui,[§,⊥] Xia Hong,[‡,§] Lan Jiang,[#] Jean-Francois Silvain,[∇] and Yongfeng Lu[*,†]

[†]Department of Electrical and Computer Engineering, University of Nebraska-Lincoln, Lincoln, Nebraska 68588-0511, United States

[‡]Department of Physics and Astronomy, University of Nebraska-Lincoln, Lincoln, Nebraska 68588-0511, United States

[§]Nebraska Center for Materials and Nanoscience, University of Nebraska-Lincoln, Lincoln, Nebraska 68588-0299, United States

[∥]Materials Science and Technology Division, Oak Ridge National Laboratory, Oak Ridge, Tennessee 37831-6124, United States

[⊥]Department of Mechanical and Materials Engineering, University of Nebraska−Lincoln, Lincoln, Nebraska 68588, United States

[#]School of Mechanical Engineering, Beijing Institute of Technology, Beijing 100081, China

[∇]Institut de Chimie de la Matière Condensée de Bordeaux, Avenue du Docteur Albert Schweitzer F-33608 Pessac Cedex, France

Supporting Information

ABSTRACT: Single-crystal transition metal dichalcogenides (TMDs) and TMD-based heterojunctions have recently attracted significant research and industrial interest owing to their intriguing optical and electrical properties. However, the lack of a simple, low-cost, environmentally friendly, synthetic method and a poor understanding of the growth mechanism post a huge challenge to implementing TMDs in practical applications. In this work, we developed a novel approach for direct formation of high-quality, monolayer and few-layer MoS_2 single crystal domains via a single-step rapid thermal processing of a sandwiched reactor with sulfur and molybdenum (Mo) film in a confined reaction space. An all-solid-phase growth mechanism was proposed and experimentally/theoretically evidenced by analyzing the surface potential and morphology mapping. Compared with the conventional chemical vapor deposition approaches, our method involves no complicated gas-phase reactant transfer or reactions and requires very small amount of solid precursors [e.g., Mo (∼3 μg)], no carrier gas, no pretreatment of the precursor, no complex equipment design, thereby facilitating a simple, low-cost, and environmentally friendly growth. Moreover, we examined the symmetry, defects, and stacking phase in as-grown MoS_2 samples using simultaneous second-harmonic-/sum-frequency-generation (SHG/SFG) imaging. For the first time, we observed that the SFG (peak intensity/position) polarization can be used as a sensitive probe to identify the orientation of TMDs' crystallographic axes. Furthermore, we fabricated ferroelectric programmable Schottky junction devices via local domain patterning using the as-grown, single-crystal monolayer MoS_2, revealing their great potential in logic and optoelectronic applications. Our strategy thus provides a simple, low-cost, and scalable path toward a wide variety of TMD single crystal growth and novel functional device design.

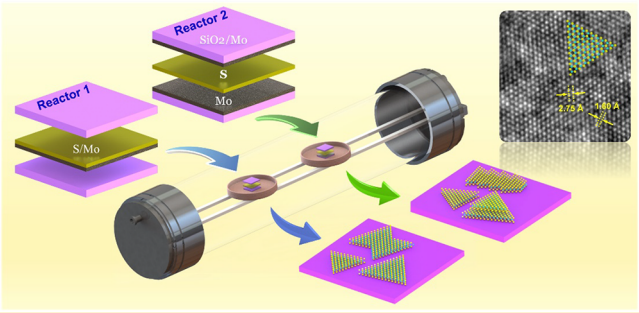

KEYWORDS: *Solid-phase sulfurization, transition metal dichalcogenides, single crystal, sum-frequency generation, heterojunction*

Atomically thin semiconducting transition metal dichalcogenides (TMDs), MX_2 (M = Mo, W; X = S, Se, Te), represent a new family of two-dimensional (2D) materials with remarkable electrical and optical properties that have attracted great scientific and industrial interests. For instance, TMD monolayers have direct/sizable semiconducting bandgaps and exhibit strong photoluminescence (PL) emissions in the visible and near-infrared spectral range.[1,2] In addition, inversion symmetry is broken for monolayer TMDs, which results in novel valley-dependent selection rules,[3−5] as well as strong nonlinear optical responses.[6−9] These unusual properties have motivated the development of monolayer TMDs for use in next-generation nano/optoelectronic devices, such as high-

Received: December 30, 2017
Published: January 19, 2018

Downloaded via UNIV OF NEBRASKA LINCOLN on February 28, 2019 at 23:02:06 (UTC).
See https://pubs.acs.org/sharingguidelines for options on how to legitimately share published articles.

 © 2018 American Chemical Society

DOI: 10.1021/acs.nanolett.7b05473
Nano Lett. 2018, 18, 2021−2032

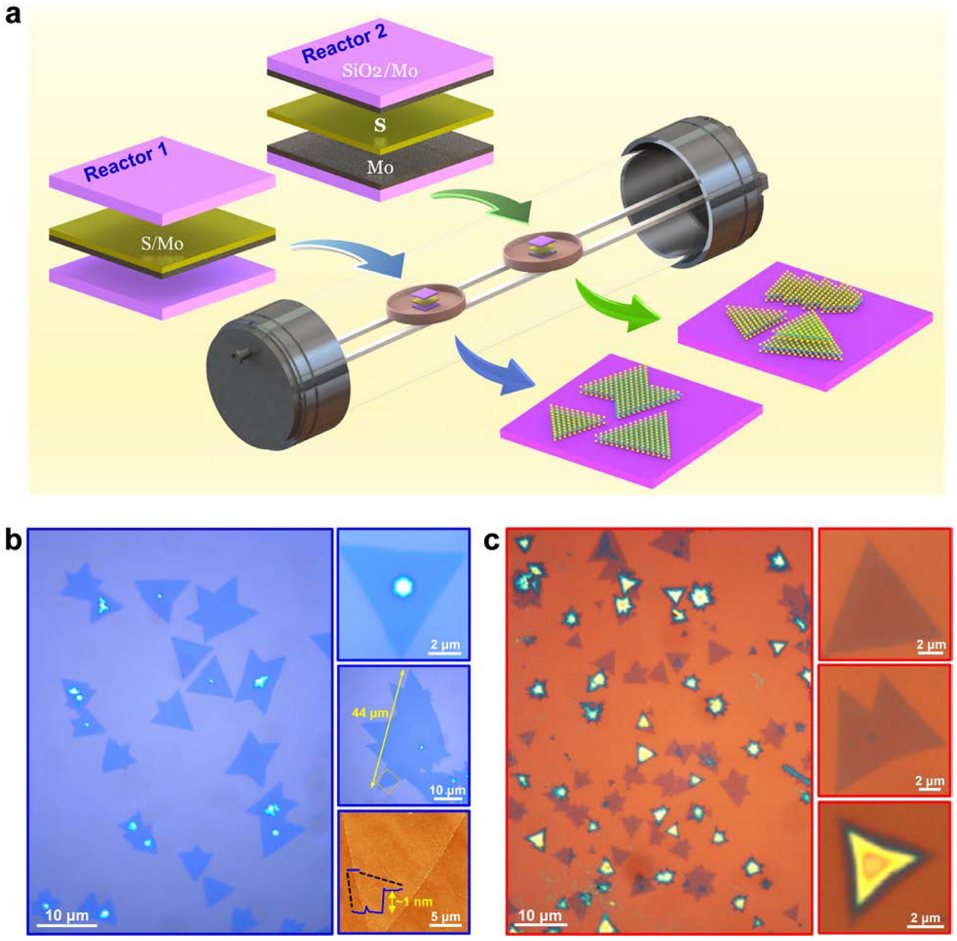

Figure 1. Growth of monolayer and few-layer MoS_2 single crystals through space-confined, solid-phase sulfurization strategy. (a) Schematic drawing of two sandwich-structured reactor configurations for space-confined solid-phase growth of highly crystalline MoS_2 atomic layers. Reactor Type 1: substrate/Mo−S/substrate. Reactor Type 2: substrate-Mo/S/Mo-substrate. (b) Typical examples of the as-grown monolayer MoS_2 grains via Reactor Type 1. Insets in (b): (top) zoomed-in optical image of a MoS_2 triangular flake with a symmetric six-lobe geometry nucleation site at the center, (middle) large-size MoS_2, and (bottom) corresponding AFM image with height profile demonstrating its monolayer characteristic. (c) Optical images of monolayer and few-layer MoS_2 samples fabricated via Reactor Type 2. The insets in (c) are zoomed-in optical images of individual MoS_2 (top, middle) monolayers and (bottom) few-layers.

performance field-effect transistors (FETs),[10−12] logic circuits,[13,14] photovoltaics and photodetectors,[15−17] sensors,[18,19] nonlinear optical devices,[20,21] spintronic devices,[4,5,22] and memristors.[23,24] Recently, considerable interest has focused on the structural phase engineering in TMDs,[25−30] which may provide a means of controlling TMD properties, leading to potential applications in novel electronic devices,[26,31] energy storage devices,[27] and catalysts.[29] Furthermore, interest in creating ultrathin semiconductor homogeneous junctions and heterojunctions based on these monolayer TMDs has also been rapidly increasing since these junctions offer unique size scaling opportunities and potential for multifunctional integration compared to conventional semiconductor devices.[32−37] Despite these highly promising features, a major challenge that limits the development of practical applications of semiconducting TMDs is the lack of a simple, low cost, environmentally friendly, and large-scale synthetic method of creating high-quality single-crystalline TMDs with controlled atomic layers.

Recently, several methods have been developed to produce atomically thin 2D TMDs, including mechanical exfoliation, liquid exfoliation, chemical vapor deposition (CVD), molecular beam epitaxy, and so forth.[38−40] Whereas the highest quality MoS_2 samples can be obtained via mechanical exfoliation from the bulk materials, which exhibit room-temperature charge mobility of >200 $cm^2\ V^{-1}\ S^{-1}$ and a high on/off current ratio (of order 10^8),[10] they are only suitable for the exploration of diverse potential as a proof of concept due to the poor yield, uncontrolled layer thickness and irregular sample geometry. In contrast, CVD has become the predominant method for cost-effective and scalable growth of TMD monolayers.[41−44] Although significant advances have been made, the fabrication of uniform and high-quality TMDs using CVD requires precise control of a series of parameters, for example, the choice of precursors, the precursor amount, the ratio of transition metal/chalcogenide reactants, the gas flow rate, the growth temperature and time, and the source−substrate configuration. Additionally, conventional CVD methods require complex processes and hardware designs of gas-phase reactant transport and chemical reactions in which the CVD process must be separately optimized for each TMD material. More specifically, the CVD growth of single-crystalline TMDs (such as MoS_2) has primarily been achieved by using vapor-phase sulfurization of transition metal oxide powders (MoO_3[44−46] or MoO_2[47]), represented by the equation: MoO_3 (MoO_2) + 3S → MoS_2 + SO_2, where the

DOI: 10.1021/acs.nanolett.7b05473
Nano Lett. 2018, 18, 2021−2032

oxygen atoms removed from MoO_3 (MoO_2) participate in forming the undesirable SO_2 gas which is extremely toxic and corrosive. In addition, if CVD chamber conditions are not properly controlled, incomplete reactions may result in uncontrolled amounts of $MoS_{2-x}O_x$ impurities in the as-grown MoS_2 crystals.[48] Furthermore, atomic oxygen is a well-known etchant for 2D materials, especially at high temperatures,[9,49] indicating that any nascent oxygen could potentially create defects/vacancies during 2D MoS_2 growth. Therefore, the use of oxygen-free molybdenum (Mo) and pure sulfur as the initial precursors could avoid the above issues and lead to rapid growth of samples with higher quality.[50] To the best of our knowledge, using ultrathin Mo film as a solid metal precursor for single crystalline MoS_2 growth has never been successfully achieved.[50−53] For example, some research groups have developed the methods to directly prepare polycrystalline MoS_2 layers on SiO_2 substrate using a predeposition of Mo (or MoO_3) films followed by CVD.[50,51,53] Additionally, sulfuring Mo foil in sulfur vapor has been reported by Tai et al. to controllably grow monolayer MoS_2 at 600 °C for 1 min,[52] whereas the formed MoS_2 layers are not single-crystal structure and also need tedious postgrowth transfer process for fabricating MoS_2-based devices. Nevertheless, the direct sulfurization of Mo film for high-quality single-crystal MoS_2 growth remains challenging.

Recently, Chen et al. demonstrated a convenient method of preparing high-quality, single crystal graphene through the design of a CVD reactor with a confined reaction space.[54] The space-confined configuration in their work provides multiple advantages, including suppressing the substrate roughness, establishing a uniform distribution of reactant concentration, and shifting the growth kinetics toward a diffusion-controlled reaction. Building on this new concept, in this work we report a novel approach to the direct formation of single crystal MoS_2 atomic layers via a single-step rapid thermal processing of a sandwich reactor with sulfur (S) and Mo film in a confined reaction space. Meanwhile, an all-solid-phase growth mechanism is proposed, as evidenced by a coupled combination of experimental measurements and first-principles calculations. In contrast to conventional CVD methods, the proposed space-confined solid-phase sulfurization strategy involves no complicated gas-phase reactant transfer or reaction and is not restricted by multiple process constrains, such as the choice of precursors, a proper vapor ratio of the Mo and S reactants, or a precise gas flow control. More importantly, contamination-free single-crystal MoS_2 can be obtained over the most of the substrate surface with very small amount of solid precursors [Mo (∼3 μg) and S (∼50 mg)], which is much less than those widely used for conventional CVD methods.[41,44,45,55] In addition, multiple 2D TMDs could be synthesized simultaneously in the same RTP furnace using the proposed space-confined sandwich reactor design (Figure 1a), which is difficult for the conventional CVD methods. Therefore, our method not only simplifies the precursor, process, and hardware design but also has less material cost and is more environmentally friendly because of minimizing the produced gas and preventing potential environmental contamination and poisonous gas leakage.

Additionally, monolayer and few-layer MoS_2 grains can be controllably grown through variations in the reactor design and conditions, thus, we were able to control the layer-thickness and stacking order of MoS_2 so as to control properties such as nonlinear optical response. We examined the symmetry, grain boundary, and stacking order of as-grown samples using simultaneous second-harmonic generation (SHG) and sum-frequency generation (SFG) imaging, which enabled fast and reliable detection of structural information. More importantly, we first observed that polarized SFG (not only peak intensity but also peak position) can also be used to determine the crystalline orientation of TMDs. Moreover, we fabricated ferroelectric programmable Schottky junction devices via local domain patterning using the as-grown monolayer MoS_2, revealing their high potential in logic and optoelectronic applications.

■ RESULTS AND DISCUSSION

Highly crystalline monolayer and few-layer MoS_2 samples were fabricated in a space-confined reactor using solid-phase sulfurization of ultrathin Mo film as a precursor, instead of the previously used MoO_3 and MoO_2 powders (Figure 1a). As illustrated in Figure 1a, two different space-confined reactors were designed and placed in the central heating zone of the rapid thermal processing (RTP) system for MoS_2 growth. For Reactor Type 1, the Mo-film-coated S plate was sandwiched in the gaps between two catalytic inactive oxides substrates (such as SiO_2/Si) (Figure S1a, Supporting Information), while for Reactor Type 2, a 0.5 mm thick S plate was sandwiched between a pair of Mo-film-coated SiO_2/Si substrates (Figure S1b, Supporting Information) (see the Methods for details). In this straightforward, one-step, solid-phase growth strategy, the creation of a space-confined configuration is capable of suppressing the sublimation of sulfur in the RTP system and increasing the nucleation probability for solid-phase growth of single crystal MoS_2 under an excessive sulfur supply.

Figure 1b shows a low-magnification optical microscope image of MoS_2 flakes grown using Reactor Type 1. By combining optical contrast and atomic force microscope (AFM) measurements, most of the as-grown MoS_2 crystals are determined to be composed of strictly a single layer. Typically, the isolated single MoS_2 crystals grown display a symmetric triangular geometry with a hexagonal nucleation site at the center (top inset in Figure 1b). The nucleus exhibits the characteristic Raman signal of thick MoS_2, E^1_{2g} at 382.2 cm^{-1} and A_{1g} at 407.1 cm^{-1} (Figure S2, Supporting Information). This result is similar to a recent report on CVD growth of monolayer $MoSe_2$,[56] indicating that the growth of MoS_2 using Reactor Type 1 could be a solid−vapor reaction involving (1) direct co-condensation and nucleation of MoS_x ($0 < x < 2$) on the substrate by Mo—S interactions and (2) sulfurization of MoS_x with local vapor-phase S to form MoS_2. Sometimes, the coalescences occur between adjacent single-crystal MoS_2 grains, resulting in the formation of monolayer MoS_2 crystals in polygonal shapes (Figure 1b and Figure S3, Supporting Information). Additionally, a large MoS_2 grain with polycrystalline geometry and an edge size of approximately 44 μm was also obtained (middle inset in Figure 1b) and confirmed to be a monolayer characteristic by AFM measurements (bottom inset in Figure 1b).

Figure 1c shows typical optical images of MoS_2 samples formed using Reactor Type 2, which exhibit several types of shapes, mainly including triangle-shaped monolayers and few-layers (Figures S4 and S5, Supporting Information), and monolayer and few-layer polygonal shapes (Figure S6, Supporting Information). In some cases, we also observed the growth of multilayer MoS_2 with various shapes and morphologies. The well-defined shapes of those polygons

DOI: 10.1021/acs.nanolett.7b05473
Nano Lett. 2018, 18, 2021−2032

indicate good crystallinity for the as-grown MoS_2 samples. It is interesting to note that no nucleation sites are visible at the center of any MoS_2 crystal, which suggests that the solid–vapor-phase growth mechanism, as mentioned above, seems unsuitable for the growth of layered MoS_2 using Reactor Type 2. The growth mechanism (solid-phase sulfurization) will be discussed later. To the best of our knowledge, this is the first time anyone has observed that solid-phase sulfurization (SPS) of ultrathin Mo film can lead to the formation of monolayer and few-layer MoS_2 single crystals.

On the basis of the above experimental observation and analysis, we can conclude that, with Type 1 reactor design (substrate/Mo–S/substrate), most of the MoS_2 samples formed on the substrate are epitaxial single layer, while Type 2 reactor design (substrate-Mo/S/Mo-substrate) offers a better yield of few-layer MoS_2 flakes, which indicates that monolayer and few-layer MoS_2 can be controllably synthesized through variations in the reactor design. More interestingly, the nucleation and growth of single crystal MoS_2 was observed to occur on both the top and bottom surfaces of the silicon substrates (Figure S7, Supporting Information). A comparison of the MoS_2 on the top and bottom surfaces indicates that, for the same reactor, MoS_2 can grow from both substrate surfaces through the same mechanism. To demonstrate the important roles of space-confined configuration, the top silicon substrate in Reactor Type 1 (or the top Mo-film-coated silicon substrate in Reactor Type 2) was removed and then annealed at 750 °C under the same conditions. The subsequent optical image and Raman analyses show the formation of continuous polycrystalline MoS_2 thin films (Figure S8, Supporting Information), while no single crystals were obtained. This outcome is attributed to the rapid sulfur evaporation and the reduced probability of nucleation for growing single-crystal MoS_2.

To study the structural phase (semiconducting 2H or metallic 1T) of the as-grown MoS_2, Raman, photoluminescence (PL), and SHG spectroscopic analyses were carried out (Figure S9, Supporting Information). Figure S9a shows the Raman spectrum taken from a monolayer MoS_2 grown via Reactor Type 1, where only two main Raman peaks of the in-plane E^1_{2g} mode and the out-of-plane A_{1g} mode, but no additional Raman signals of the J_1, J_2, and J_3 originated from the 1T phase MoS_2, can be seen.[57,58] This Raman feature indicates that the as-grown monolayer MoS_2 via Reactor Type 1 is semiconducting 2H phase. PL analysis in Figure S9b reveals that this monolayer MoS_2 is highly photoluminescent, with a PL energy of about 1.85 eV, which is consistent with a direct band gap structure of monolayer 2H phase MoS_2 (1.8–1.9 eV).[1,2] SHG spectroscopy imaging can also be used to distinguish 2H and 1T phase in monolayer TMDs, because the inversion symmetry is broken in the 2H phase but present in the 1T phase.[31] As expected, a strong SHG signal was observed over the entire monolayer MoS_2 (Figure S9c), further confirming the formation of 2H structural phase. In addition, we found that the MoS_2 samples grown using Reactor Type 2 behavior almost the same in Raman, PL, and SHG optical properties compared to the MoS_2 grown using Reactor Type 1 (Figure S9d–f). Taken together, the above analyses indicate that the space-confined SPS strategy favors the formation of high-quality, thermodynamically stable 2H phase MoS_2 single crystals.

As is known that the ability to control the physical properties of the as-grown MoS_2 layers via phase engineering is very important for next generation novel device applications,[25,26,59] which has been so far realized by lithium intercalation,[28,29,59] electron beam irradiation,[60] and plasmonic hot electrons.[58] In particular, Chang et al. realized the selective synthesis of 2H- and 1T-phase MoS_2 monolayers at different annealing temperature by employing lithium molten salts (e.g., LiOH).[29] Building on this work, it is also possible for us to control the different phases of MoS_2 single crystals by rapid thermal processing of a sandwich reactor with LiOH, S, and Mo films in a confined reaction space, which needs an in-depth study in the future. It is expected that 2H phase MoS_2 could be obtained at a relatively low temperature (≤750 °C), while a phase transition in MoS_2 from 2H to 1T by lithium intercalation will occur when the processing temperature is over 1000 °C, leading to the formation of 1T-phase MoS_2.

To further study the phase purity and crystal quality of the as-grown MoS_2 crystals, high-resolution transmission electron microscopy (HR-TEM) characterization was performed to obtain a direct observation of their atomic structures. Figure 2a

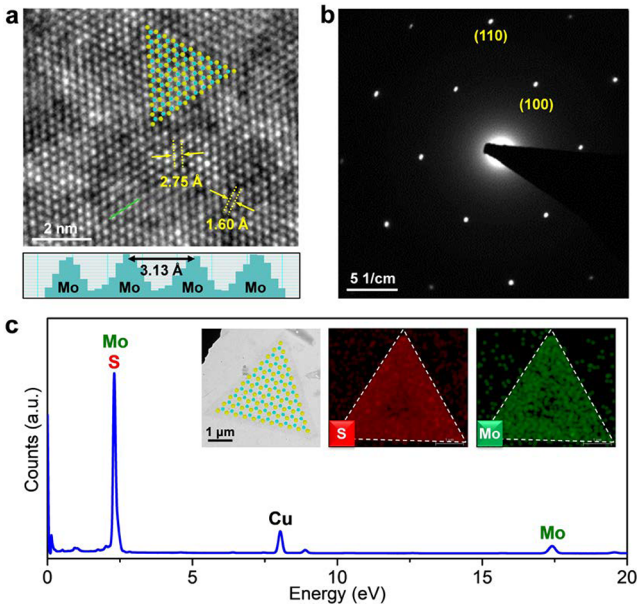

Figure 2. Structural and crystalline quality characterization of the as-grown single-crystal MoS_2 domains. (a) High-resolution TEM image of the as-grown MoS_2 single crystal with a schematic of the atomic positions, where the bright spots correspond to Mo atoms. Inset: cross-sectional intensity profile along the green line in (a). (b) SAED pattern of the as-grown MoS_2 single crystal, confirming the pure 2H phase structure. (c) EDS spectrum collected from the as-grown MoS_2 single crystal. Inset: low-resolution TEM image of the same sample and the corresponding elemental mapping of S (red) and Mo (green).

shows a typical high-resolution TEM image of the as-grown MoS_2 single crystal with a schematic of the atomic positions, where the uniformly distributed bright spots correspond to Mo atoms but S atoms are not evident due to their smaller electron cross section.[45,61] The lateral intensity profile along the green line in Figure 2a reveals a Mo—Mo (or S—S) bond distance of 3.13 Å for the MoS_2 crystals. One can also see that the as-grown MoS_2 has a hexagonal phase structure with measured lattice distances of 2.75 and 1.60 Å, which correspond to those of (100) and (110) planes of 2H-MoS_2 monolayers.[62] Additionally, no obvious defects, such as dislocations, interstitials, or vacancies, are observed over the whole sample region, demonstrating that the grown MoS_2 single crystals via

DOI: 10.1021/acs.nanolett.7b05473
Nano Lett. 2018, 18, 2021–2032

all-solid state reaction method have very high 2H phase purity and crystallinity. The selected-area electron diffraction (SAED) pattern displayed in Figure 2b clearly shows a single set of diffraction peaks with the hexagonal symmetry, which is consistent with the result obtained from fast Fourier transform (FFT) pattern analysis (Figure S10, Supporting Information), further confirming that it is a single crystal with 2H phase structure in the as-grown sample. In addition, energy-dispersive X-ray spectrometry (EDS) and elemental mapping analyses were performed to identify the chemical composition and uniformity of the as-grown 2D crystals (Figure 2c), which reveals that the as-grown MoS_2 is only composed of Mo and S with a Mo:S atomic ratio of about 1:2.03, without the presence of any other impurities, indicating that the as-grown 2H phase MoS_2 has good stoichiometry.

To improve the preparation of high-quality layered MoS_2, we will learn more about the single crystalline grain growth process. As has been mentioned above, monolayer and few-layer MoS_2 crystals grown using Reactor Type 2 were realized by direct sulfurization of solid-phase Mo film deposited on silicon substrate in a space-confined configuration, which is different from the generally accepted vapor-phase[41,44,51,63] or solid−vapor phase[56] reaction mechanism for CVD growth of monolayer TMDs. To better understand its growth mechanism, the intermediate phases in quenched MoS_2 samples at the initial stage were analyzed via AFM and KPFM. Figure 3a_1−d_1 shows optical images of the triangular-shaped MoS_2 formed with four different degrees of sulfurization. Initially, small triangular-shaped MoS_2 grains are appreciated and nucleated from Mo film by sulfurization, leading to the formation of holes on silicon substrate, as shown in Figure 3a_2−d_2. It is surprising that the hole is much deeper (in the range of 8−25 nm) than the thickness of the Mo film (2−5 nm), indicating that a thick sulfur coating layer is deposited on the Mo film surface at the initial growth stage. As the sulfurization evolves over time, the depths and sizes of the holes continue to increase, resulting in larger single-crystal MoS_2. More interestingly, it is observed that the crystalline edges of MoS_2 grains in the hole are surrounded by a triangular border with a gradient thickness (increasing from the inner to the outer edge) approximately from 300 to 500 nm in width (see insets in Figure 3a_2−d_2), which is consistent with a TEM observation of the crystal boundary (Figure S11, Supporting Information). We surmise that the gradual height changing profiles of the triangular ring that were observed are correlated with the in-plane "feedstock" condition of the sulfur source, where the inner edge provides more sulfur for single-crystal MoS_2 growth, which results in the surrounding ring edge being "etched away".

From the corresponding KPFM imaging, as shown in Figure 3a_3−d_3, the surface potential or the potential difference (ΔPD) between the as-grown MoS_2 and the substrate are also found to strongly depend on the sulfurization degree, namely, MoS_2 with the different degrees of sulfurization corresponds to different work functions. We find that the more the amount of MoS_x ($0 < x \leq 2$) (or the higher crystallinity), the larger the surface potential values for MoS_2 nucleations. The work function of MoS_x can be calculated using the following equations[64]

$$\phi_{MoS_2} = \phi_{tip} - e(CPD_{tip} - CPD_{MoS_2}) \quad (1)$$

$$\phi_{Substrate} = \phi_{tip} - e(CPD_{tip} - CPD_{Substrate}) \quad (2)$$

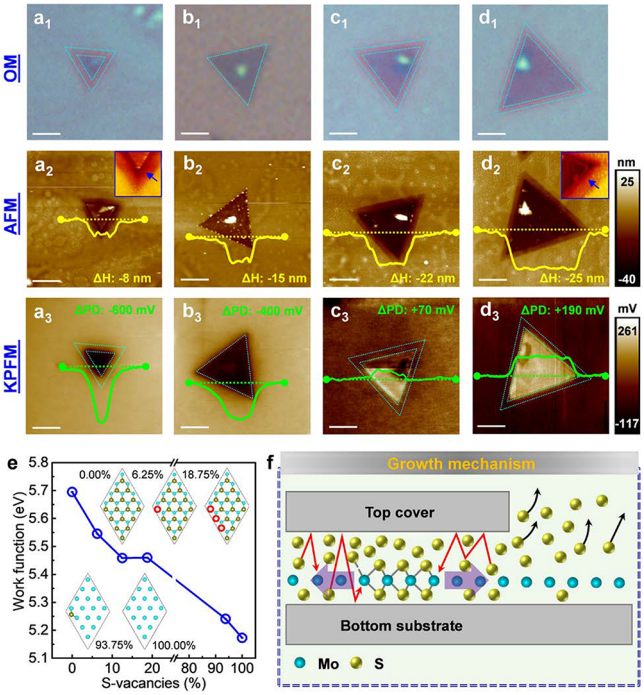

Figure 3. Solid-phase reaction growth mechanism of monolayer MoS_2 single crystal domains. (a_1−d_1) Typical optical images showing the initial growth of triangular-shaped MoS_2 with different degrees of sulfurization. (a_2−d_2) AFM height topographies of corresponding samples in (a_1−d_1). Insets in (a_2−d_2) shows the height profiles along the yellow dashed lines. The top-right insets in (a_2,d_2) present the magnifying edge areas, where the as-grown MoS_2 grains are pointed by the blue arrows, and a broad transition area is clearly observed. (a_3−d_3) KPFM imaging of corresponding samples in (a_1−d_1). Insets in (a_3−d_3) show line-scan surface potential profiles along the green lines. Scale bars: 2 μm. (e) The work functions of monolayer MoS_2 with respect to the sulfur (S)-vacancy concentration. Inset: structural models for monolayer MoS_2 with different concentrations of S-vacancies. (f) Schematic illustration showing the proposed space-confined solid-phase sulfurization reaction mechanism. Red arrows represent sulfur atom rebounce in the confined reaction space, black arrows indicate rapid sulfur evaporation without top cover, and broad purple arrows indicate lateral epitaxial growth in the confined region.

$$\phi_{MoS_2} = \phi_{Substrate} + e\cdot(CPD_{MoS_2} - CPD_{Substrate}) = \phi_{Substrate} + e\Delta PD \quad (3)$$

where ϕ_{MoS_2}, ϕ_{tip}, and $\phi_{Substrate}$ represent the work functions of the MoS_2, Pt−Ir tip, and substrate; CPD_{MoS_2}, CPD_{tip}, and $CPD_{Substrate}$ are the corresponding surface potentials. From eq 3 and the above observed surface potential variation, we can conclude that the work function of MoS_2 increases with the increment (or decrement) in the sulfurization degree (or S-vacancy concentration). The work function of monolayer MoS_2 as a function of S-vacancy concentration has been further validated using ab initio calculations (Figure S12, Supporting Information). Consistent with the experimental results, the work function of monolayer MoS_2 decreases with S-vacancy concentration (Figure 3e).

Considering the above AFM and KPFM analyses, the growth of single-crystal MoS_2 under these conditions could be an all-solid-phase reaction, where the solid Mo film and solid S film served as reactants. We, therefore, propose a multistep growth model for monolayer MoS_2, depicted in Figure S13,

DOI: 10.1021/acs.nanolett.7b05473
Nano Lett. 2018, 18, 2021−2032

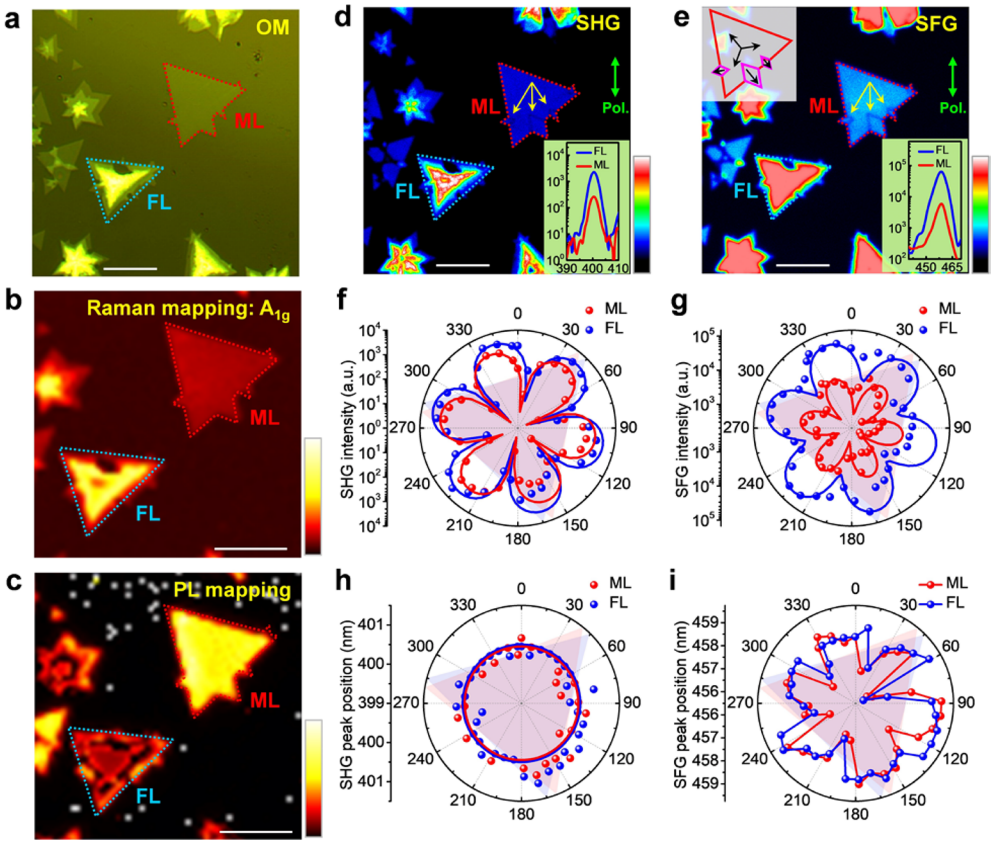

Figure 4. Optical quality evaluation of the as-grown SPS MoS_2 samples. (a) Optical image of the as-grown MoS_2 flakes with different layer thicknesses after transference onto fused silica. The dashed lines in red and blue depict the MoS_2 monolayer and few-layer, respectively. (b−e) (b) Raman intensity mapping of the A_{1g} band, (c) PL peak intensity mapping from the A° exciton, (d) SHG imaging, and (e) SFG imaging of the as-grown monolayer and few-layer MoS_2 in the same area as shown in (a). The insets in (d,e) compare the nonlinear optical signals of (d) SHG and (e) SFG for the monolayer and few-layer MoS_2, where the red and blue curves refer to monolayer and few-layer MoS_2, respectively. (f,g) The polar plots of the parallel polarization (f) SHG and (g) SFG intensity as a function of monolayer and few-layer MoS_2 rotation angle. (h,i) The polar plots of the parallel polarization (h) SHG and (i) SFG peak position as a function of monolayer and few-layer MoS_2 rotation angle. Scale bars: 10 μm.

based on the space-confined solid-phase sulfurization reaction mechanism (Figure 3f). The first step is physical adsorption of a thick layer of sulfur coating on the Mo-film-coated substrate during the ramp up to the reaction temperature to provide the excess of sulfur precursor. The second step is the nucleation by sulfurization of Mo film, involving Mo−S bond formation, lattice reorganization, and triangular island formation. During the nucleation (second step) and epitaxial growth (third step) processes, the top cover in sandwich reactor plays important roles of 1) increasing the interaction between Mo and S atoms, and 2) physically confining the sulfur precursor in the spaces between the top structure and the bottom substrate to suppress the sulfur sublimation, thereby keeping the excessive amounts of sulfur, which are beneficial for the nucleation and epitaxial growth of MoS_2 (Figure 3f). However, for reactor design without the top cover (Figure 3f), it may lead to the reduced concentration of sulfur precursor and the decreased interaction between Mo and S atoms, thereby resulting in the formation of polycrystalline or amorphous MoS_2 films (Figure S8, Supporting Information). With the growth time increased (third step), the small-grain MoS_2 expands outward from the nucleation sites to form large crystals by in-plane diffusion of the Mo and S feedstocks from the surrounding Mo film/S coating. Different from conventional CVD growth, the Mo film not only serves as the local Mo source but also serves as the nucleation site for the in situ sulfurization, which determines the final MoS_2 growth position. Finally, the growth stops when the precursor sources, including Mo and S, are completely evaporated and exhausted.[65] The formation of isolated MoS_2 crystals but not continuous highly crystalline films is likely due to the multinucleation but no epitaxy to line up the crystals.

It is known that 2D materials show strong layer-thickness- and stacking-phase-dependent optical properties. Therefore, the as-grown monolayer and few-layer MoS_2 samples enables us to observe the unique layer-thickness- and stacking-phase-dependent nonlinear optical responses that have not been previously reported in mechanically exfoliated MoS_2 samples.[6] Figure 4a shows a representative optical image of as-grown MoS_2 grains with different layer thicknesses transferred onto a fused silica wafer. The number of atomic layers is first verified via AFM analysis (Figure S14a,b, Supporting Information), where the two triangular MoS_2 flakes, marked by dashed lines in red and blue, correspond to one atomic layer (monolayer sample) and roughly 10 monolayers (few-layer sample), respectively. Moreover, by combining the examination of the Raman frequency difference between the E^1_{2g} (in-plane vibration) and A_{1g} (out-of-plane vibration) modes and the PL peak intensity, we further confirm their monolayer and few-layer characteristics (Figure S14c,d, Supporting Information). In addition, Raman and PL mappings are performed to examine the spatial uniformity. As shown in Figure 4b, the excellent uniformity of the Raman A_{1g} peak intensity mapping

DOI: 10.1021/acs.nanolett.7b05473
Nano Lett. 2018, 18, 2021−2032

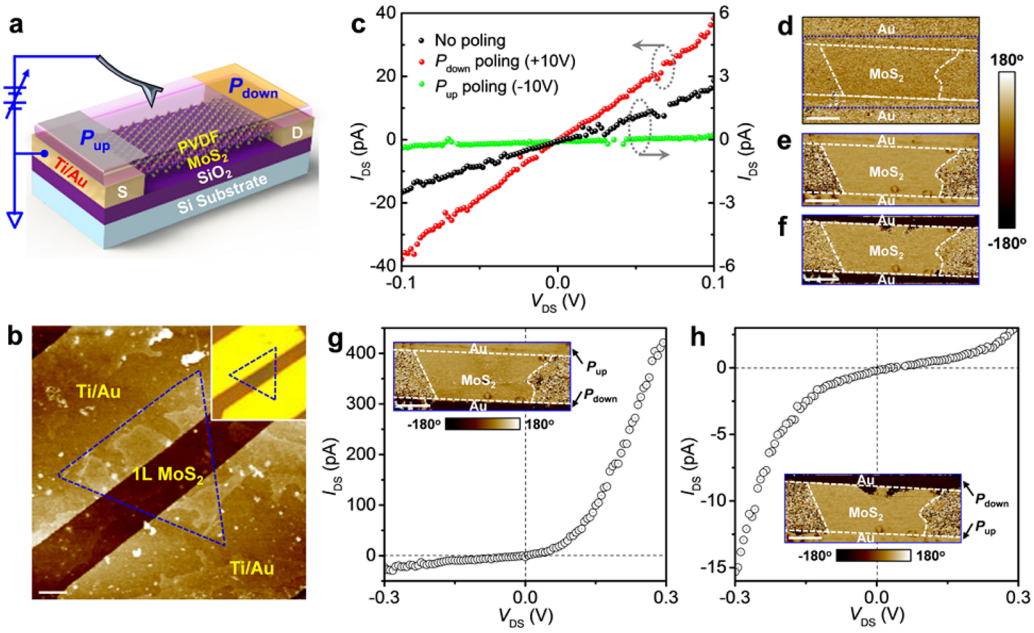

Figure 5. The fabrication and characterization of a programmable monolayer MoS_2−metal heterojunction via ferroelectric domain patterning. (a) Schematic of the MoS_2-metal heterojunction construction process. (b) AFM topography and optical image (inset) of a fabricated monolayer MoS_2 device with a 20 nm PVDF-TrFE top-layer. Scale bar: 1 μm. (c) Room-temperature $I_{DS}-V_{DS}$ characteristics for sample in (b) in the initial unpoled state (black), and after uniformly poling the ferroelectric top-layer via a conductive AFM tip with a bias voltage of +10 V (red) and then poling the contact areas with −10 V (green). (d−f) The corresponding PFM phase images (d) in the initial state and after poling with a tip bias of (e) +10 V and (f) −10 V. Scale bars: 1 μm. (g,h) Room-temperature $I_{DS}-V_{DS}$ characteristics of the same device at the (g) P_{down}(upper electrode)−P_{up}(lower electrode) state and (h) P_{up}(upper electrode)−P_{down}(lower electrode) state, respectively. Insets: PFM phase images. Scale bars: 1 μm.

reflects the high degree of uniformity within both monolayer and few-layer MoS_2 samples. A similar degree of uniformity could also be observed from the PL mapping of the A° exciton, as shown in Figure 4c. It should be noted that significant variations in PL intensity are observed close to the grain edges of few-layer MoS_2, indicating structural defects (e.g., sulfur vacancies)[66] or thickness variations at the edge regime. In general, all of the characterizations based on Raman and PL spectroscopy suggest the uniformity and high optical quality of the as-grown samples.

We next investigate more structural information about these samples using multimodal nonlinear microscopy, as described in the Experimental Section.[9] Figure 4d,e show the simultaneous SHG and SFG imaging of the same region shown in (a), including monolayer and few-layer (up to 10 layers) MoS_2 crystals. The contrasts of both SHG and SFG are similar, as both modalities are sensitive to the elements of second-order nonlinearity $\chi^{(2)}$. Features seen in the SHG image are reproduced in the SFG image. For example, both the SHG and SFG images for monolayer MoS_2 show a suppressed nonlinear optical signal intensity at the points indicated by three yellow arrows (Figure 4d,e), revealing its polycrystalline nature and opposite orientation between adjacent grains (top inset in Figure 4e). The suppressed SHG and SFG at the grain boundaries is attributed to the destructive interference and annihilation of the nonlinear waves generated from the neighboring grains with opposite orientation.[67] These grain boundaries, however, cannot be identified using Raman and PL mapping or AFM (Figure S14a, Supporting Information), demonstrating the capability of direct visualization of the grain structures in MoS_2 via not only the SHG[67] but also the SFG imaging techniques.

Second-order optical nonlinearity, which is responsible for both SHG and SFG, is very sensitive to the thickness of TMDs due to their inversion symmetry variation. It is known that the lack of an inversion center in monolayer or few-layer TMD samples with an odd number of layers leads to strong second-order optical responses, while TMDs with an even number of layers produce no second-order signals.[6,9] Here, the enhanced SHG and SFG signals from few-layer MoS_2 are observed, which are substantially more than a magnitude stronger than those from the monolayer MoS_2 (insets in Figure 4d,e). This is surprising, since one normally expects the intensities of nonlinear SHG and SFG signals to exponentially decrease with the number of layers.[6,9] The stronger SHG and SFG responses in few-layer MoS_2 can be attributed to the absence of an inversion center, namely, the results of the AA (the in-plane Mo—S bond is the same for the adjacent layers) stacking configuration in this few-layer sample, which is different from the naturally few-layer MoS_2 with AB (the in-plane Mo−S bond is opposite for the adjacent layers) stacking. Quantitatively, similar to the artificially stacked TMD bilayers,[68] the SHG and SFG fields in the as-grown few-layer MoS_2 can be modeled as a coherent superposition of the SHG and SFG fields from the individual layers. Then, the SHG and SFG intensities in the AA stacking, few-layer MoS_2 can be expressed as $I^n_{SHG} = \left|\sum_{k=1}^{n} \vec{E}_k(2\omega_{probe})\right|^2 = n^2 I^1_{SHG}$ and $I^n_{SFG} = \left|\sum_{k=1}^{n} \vec{E}_k(\omega_{probe} + \omega_{pump})\right|^2 = n^2 I^1_{SFG}$, where I^n_{SHG}, I^n_{SFG}, I^1_{SHG}, I^1_{SFG}, and n represent SHG and SFG intensities in few-layer MoS_2, SHG, and SFG intensities in monolayer MoS_2, and layer number, respectively. However, both the measured SHG and SFG intensities were somewhat lower than the above model prediction, which might be due to the inconsideration of the propagating effects of electromagnetic waves through the

DOI: 10.1021/acs.nanolett.7b05473
Nano Lett. 2018, 18, 2021−2032

MoS_2 layers and the substrate. In some cases, we also observed the growth of AB stacking, few-layer MoS_2, which is easily identified via SHG and SFG imaging (Figure S15, Supporting Information). Nonetheless, both SHG and SFG imaging are reliable in rapidly distinguishing the AA, AB, and even more complex stacking orders in the as-grown few-layer MoS_2.

Moreover, the crystal orientation of monolayer and few-layer MoS_2 crystals is investigated using polarization-resolved SHG and SFG. The incident laser beam is labeled with a green arrow (Figure 4d,e). The parallel polarization of SHG intensity is found to exhibit a 6-fold rotational symmetry in both monolayer and few-layer MoS_2, which reflects the 3-fold rotational symmetry of these crystals (Figure 4f).[6] The orientation of each SHG intensity maximum (or minimum) pointed to the armchair (or zigzag) direction in monolayer and few-layer MoS_2 samples (Figure S16, Supporting Information).[69] Figure 4g presents a polar plot of SFG peak intensity from monolayer and few-layer MoS_2, where a clear, coherent, and 6-fold symmetry is observed in both monolayer and few-layer regions. This result is consistent with SHG polarization dependence measurement, suggesting that SFG polarization can also be used to determine TMD structural symmetry.

Figure 4h,i compares the polar plots of the parallel polarization (h) SHG and (i) SFG peak position as a function of monolayer and few-layer MoS_2 rotation angle. Interestingly, the polarized SFG peak position also shows a characteristic 6-fold pattern (Figure 4i), similar to that of SHG and SFG intensity polarization dependence (Figure 4f,g). A similar phenomenon is also observed in the mechanically exfoliated few-layer MoS_2 samples (Figure S17, Supporting Information). In contrast, the peak position of polarized SHG emission is independent of crystal orientation (Figure 4h). By rotating the sample, the SFG peak position blue shifts and a minimum wavelength is obtained when the zigzag direction is parallel to the incident polarization. It then rapidly red shifts and reaches a constant position when the bisector of the triangular is roughly parallel to the incident polarization, which indicates that the SFG peak position is tunable and more sensitive to the MoS_2 zigzag configuration. Such tunability may arise from the selective absorption and coupling of fundamental beams with different wavelengths, demonstrating a new platform for frequency converters (or optical switches) based on 2D TMDs. To the best of our knowledge, this is the first observation that SFG (not only peak intensity but also peak position) polarization can also be established as a precise optical method of determining the orientation of crystallographic axes of TMDs.

In order to demonstrate the technological potential of the as-grown SPS monolayer MoS_2 for logic and optoelectronic applications, we designed a programmable MoS_2-metal Schottky junction device by contact engineering via local ferroelectric domain patterning (Figure 5a). We deposited a thin layer ferroelectric polymer, poly(vinylidene fluoride-trifluoroethylene) (PVDF-TrFE), on a MoS_2 device (Figure 5b), using its out of plane polarization to control the Fermi level in MoS_2, which in turn can modulate the contact potential between MoS_2 and the metal contact (Ti/Au). Figure 5c compares the source-drain current−voltage ($I_{DS}-V_{DS}$) relation of the sample (Figure 5b) in the initial unpoled state of PVDF-TrFE, and after poling the ferroelectric top-layer via a conductive AFM tip with either a positive (+10 V) or negative (−10 V) bias voltage, resulting in the polarization down (P_{down}) or polarization up (P_{up}) states, respectively. In Figure 5e, we poled the entire device area with a tip bias of +10 V. Compared with the unpoled state (Figure 5d), the channel conduction increases significantly, as the P_{down} state accumulates electrons into MoS_2, raising the Fermi level of MoS_2 toward the conduction band edge. We then poled the two contact areas with −10 V tip bias, while keeping the ferroelectric polymer above the MoS_2 remaining in the P_{down} state (Figure 5f). Surprisingly, the two-point conduction decreases drastically, which is attributed to an enhanced contact potential between MoS_2 and metal electrodes. We have thus achieved a nonvolatile current switching ratio of approximately 150 between the P_{down} and P_{up} states of contact doping. In all three states, we observed linear, Ohmic $I_{DS}-V_{DS}$ characteristics, indicating the symmetric configuration of the MoS_2 device.

On the basis of the above experimental results, we created the monolayer MoS_2 heterojunction by asymmetric contact doping, poling the upper electrode to the P_{down} state and the lower electrode to the P_{up} state (Figure 5g inset). The device then exhibits a rectified $I_{DS}-V_{DS}$ relation with a forward to reverse current ratio in excess of approximately 20 at ±0.3 V. The diode-like $I_{DS}-V_{DS}$ relationship can be well described by the thermionic emission model[70]

$$J_{DS} = J_0 \exp\left(\frac{qV_{DS}}{\eta k_B T}\right)\left[1 - \exp\left(-\frac{qV_{DS}}{k_B T}\right)\right] \tag{4}$$

where q is the electron charge, k_B is the Boltzmann constant, η is the ideality factor which is normally between 1 and 2, and J_0 is the saturation current density, given as

$$J_0 = A^*_{2D} T^{3/2} \exp\left(-\frac{q\phi_B^{eff}}{k_B T}\right) \tag{5}$$

with $A^*_{2D}=[(qm_c k_B^{3/2})/(\pi\hbar^2)](m_t^*/2\pi)^{1/2}$. Here A^*_{2D} is the 2D effective Richardson constant, m_c is the number of equivalent conduction band minima, m_t^* is the transverse electron effective mass for MoS_2, and ϕ_B^{eff} is the effective Schottky barrier height. An ideality factor η = 1.40 at room temperature is extracted from eq 4. From eq 5, the Schottky barrier height ϕ_B^{eff}corresponding to the difference in Fermi level between the two poling states is determined to be approximately 530 meV, which is much larger than other 2D MoS_2-based homojunction devices.[36,71]

More interestingly, if we reverse the poling configuration between two contacts, that is, poling the upper electrode to be P_{up} and the lower electrode to be P_{down} (Figure 5h), we observed a rectified $I_{DS}-V_{DS}$ behavior with an opposite polarity. We interpreted this phenomenon as the contact modulation. When one electrode is poled down, more electrons are doped into the Ti-MoS_2 contact which makes the contact to be an Ohmic type, while if the other electrode is configured to be P_{up} state, a depletion happened in the contact region, thus forming a Ti−MoS_2 (metal−semiconductor) Schottky junction. This mechanism naturally explains the rectified $I_{DS}-V_{DS}$ behavior formation and its polarity reversal phenomenon after changing it from Ti−MoS_2 junction to MoS_2−Ti junction. This experiment provides an example for well-controlled, reconfigurable modulation of the contact type in 2D materials electronics through the ferroelectric domain patterning.[37] Overall, the successful creation of novel functional devices using the as-grown, high-quality single-crystalline

DOI: 10.1021/acs.nanolett.7b05473
Nano Lett. 2018, 18, 2021−2032

MoS_2 will enable ultrathin, high-performance advanced electronics and optoelectronics.

CONCLUSIONS

In summary, we have demonstrated a facial single-step strategy for synthesizing high-quality monolayer and few-layer crystals of the transition-metal dichalcogenide MoS_2 by solid-phase sulfurization of Mo film in a 2D confined reaction space. Using this unique method, single-crystalline MoS_2 can be obtained without the added cost, time, and complexity (in precursor, process, and hardware designs) typically required for growth by chemical vapor deposition. We followed evolution of MoS_2 crystal growth through imaging by atomic force microscopy and Kelvin-probe force microscopy and found an unusual dependence between sulfurization degree and surface morphology or potential, based on which an all-solid-phase synthesis mechanism was proposed. In addition, we examined the symmetry, grain boundary, and stacking orders of as-grown samples using second-harmonic generation and sum-frequency generation nonlinear optical imaging, and report for the first time that the dependence of the SFG peak intensity and position on optical polarization direction can be used for a reliable, simple, and noninvasive determination of crystal orientation. Moreover, monolayer SPS MoS_2-based ferroelectric programmable Schottky junction devices via local domain patterning were successfully fabricated and shown to have excellent nonvolatile modulation characteristics, thus demonstrating their high potential in 2D logic and optoelectronic applications. Our strategy might be universal and readily applicable to a large class of 2D TMD single crystals, which is a big step toward both fundamental research and practical applications in novel nanoelectronics and optoelectronics.

METHODS

MoS_2 Single Crystal Growth. The growth of single-crystal MoS_2 was carried out using an rapid thermal processing (RTP) system (MTI, OTF-1200X-4-RTP) within a specially designed, sandwiched reactor with a sulfur plate and Mo film in a confined reaction space (Figure S1, Supporting Information). Two sandwich-structured reactors were designed and fabricated. [Reactor Type 1 (Figure S1a): A thick plate of sulfur (10 mm × 5 mm × 0.5 mm) (Aldrich, 99.998%) was deposited with a Mo film of approximately 3 nm by direct current (DC) magnetron sputtering using a Mo target at room temperature. The Mo-coated S plate was then embedded between two 300 nm-thick silicon substrates to form a substrate/Mo—S/substrate sandwiched structure. Reactor Type 2 (Figure S1b): both the top and bottom silicon substrates (area, ∼1 cm^2) were deposited with Mo by DC sputtering to a thickness in the range of 3−5 nm. Then, a sulfur plate approximately 0.5 mm was placed between two Mo-coated silicon substrates to form a substrate-Mo/S/Mo-substrate sandwiched structure. The weight of the deposited of Mo film was calculated to be ∼3 μg, and the sulfur plate used was ∼50 mg. The sandwich-structure reactors were loaded into the central heating zone of an RTP system, and then the RTP tube was purged with Ar gas to remove the air from the tube. Next, the RTP tube was pumped down and maintained at approximately 2 Torr. The temperature of the RTP tube was rapidly increased from room temperature to 750 °C at a rate of 500 °C min^{-1}, kept at 750 °C for 5 to 10 min, and then cooled down to room temperature. The growth temperature and time used in this work are comparable with those generally required for conventional CVD methods.[41,55,72,73]

The Fabrication of Programmable Monolayer MoS_2−Metal Heterojunctions. First, monolayer MoS_2 device with two-probe geometry was fabricated via standard photolithography and e-beam evaporation using the Ti/Au (5/50 nm) as the contacts. Second, a thin layer ferroelectric polymer, PVDF-TrFE with a thickness of approximately 20 nm, was coated on the monolayer MoS_2 device by horizontal Langmuir−Blodgett (LB) deposition technique.[74,75] Finally, the ferroelectric domain patterns were written via the conductive AFM. Note that bipolar polarization patterns can be prepared on the sample with very stable polarization state up to 7 weeks with no significant decay of polarization.[76]

Micro-Raman and PL Measurements. Raman and PL spectroscopy was performed in a micro-Raman spectrometer (InVia plus, Renishaw, Gloucetershire, U.K.) using a 50× objective lens. The excitation source used was an Ar^+ laser with a wavelength of 514.5 nm, a power of approximately 1.5 mW, and a spot size of approximately 1 μm^2.

Multiphoton Nonlinear Optical Spectroscopy Measurements. The nonlinear optical properties of as-grown MoS_2 samples were investigated using a previously described multiphoton nonlinear optical microscopy system.[9,77] A commercial Ti:sapphire femtosecond laser (MaiTai DeepSee HP, SpectraPhysics) (central wavelength, 800 nm; pulse duration, 100 fs; repetition, 80 MHz) in conjunction with a supercontinuum generator (SCG-800, Newport) provided two incident laser beams: pump light and probe light. The pump and probe laser beams were then focused collinearly onto the sample surfaces using a water-immersion objective lens. The multimodal nonlinear optical imaging signals were detected using multichannel photomultiplier tubes (PMTs) in the epi direction, while the nonlinear optical spectra were collected using a spectrometer in the forward direction. For polarization-dependent nonlinear optical spectral measurement, a polarizer was placed in front of a spectrometer and parallel to the polarization of the incident pump−probe beams. The angular dependence of the nonlinear optical signal was measured by rotating the samples with steps of 10°.

AFM and KPFM Measurements. The AFM and KPFM images were obtained using a Bruker Multimode 8 AFM system. An AFM tip (SCANASYST-AIR, Bruker Nano Inc., U.S.A.) was applied to probe the topography and thickness of the samples in the peak-force working mode, while the KPFM measurements were performed using a conductive tip (SCM-PIT, Bruker, U.S.A.) with a resonant frequency of 75 kHz, a lift height of 20 nm, and the ac bias of 0.5 V.

TEM Measurements. The crystalline quality of as-grown MoS_2 crystals was evaluated using a transmission electron microscope (TEM, Tecnai Osiris S/TEM, FEI, U.S.A.) operated at acceleration voltage of 200 kV, equipped with a super-X windowless EDS detector.

Theoretical Calculations. The first-principles calculations were performed using projected augmented wave (PAW)[78] method as implemented in Vienna ab initio Simulation Package (VASP).[79] The cutoff energy for plane wave is selected to be 520 eV. A Γ-center 4 × 4 × 1 Monkhorst−Pack[80] K-mesh is employed for Brillouin zone integration. Supercell method is used for the defects (S-vacancy). We first construct a monolayer MoS_2, periodic in-plane yet be

DOI: 10.1021/acs.nanolett.7b05473
Nano Lett. 2018, 18, 2021−2032

separated by a vacuum layer along *c*-direction. The S atoms are removed gradually and symmetrically above and below Mo layer. Because it has been shown that sulfur vacancies on MoS_2 tend to form line defect,[81] we simply assume the vacancies form a row (Figure S12a). The ionic relaxation is performed in the presence of defects using quasi-Newton method, and the Hellmann−Feynman forces are converged to 0.005 eV/Å. In addition, for pure compound (monolayer Mo and monolayer MoS_2), the structure is fully optimized. The layer-averaged electrostatic potential, including both Hartree energy and Ewald energy, is illustrated in Figure S12b. Work function is computed by comparing the electrostatic potential of vacuum and the Fermi level, extracted from ab initio (Figure S12c).

■ ASSOCIATED CONTENT

Supporting Information

The Supporting Information is available free of charge on the ACS Publications website at DOI: 10.1021/acs.nanolett.7b05473.

Preparation of sandwich-structured reactors for 2D MoS_2 growth; optical characterization of as-grown monolayer MoS_2 triangular flake via reactor type 1; typical examples of MoS_2 samples grown via reactor type 1; optical characterization of as-grown monolayer MoS_2 flake via reactor type 2; optical characterization of as-grown few-layer MoS_2 flake via reactor Type 2; typical examples of MoS_2 samples grown via reactor type 2; atomic layered MoS_2 grown on the top and bottom SiO_2/Si substrates; MoS_2 thin films grown via two reactors without top covers; phase identification of as-grown MoS_2 samples via solid-phase sulfurization; TEM image and FFT pattern collected from the as-grown single-crystal MoS_2 domains; TEM characterization of the MoS_2 grain quenched at the initial growth stage; theoretical calculation of the effect of sulfur vacancies on the work function of MoS_2; a multistep growth model based on the space-confined solid-phase sulfurization; AFM characterization of the monolayer and few-layer MoS_2; SHG and SFG imaging of AA- and AB-stacked few-layer MoS_2; determination of crystal orientation of as-grown MoS_2 flake; determination of crystal orientation of mechanically exfoliated MoS_2 crystals (PDF)

■ AUTHOR INFORMATION

Corresponding Authors

*E-mail: ylu2@unl.edu.

*E-mail: lidawei1008@gmail.com.

ORCID

Dawei Li: 0000-0001-6967-4968

Stephen Ducharme: 0000-0003-0936-7995

Xia Hong: 0000-0002-7873-5774

Lan Jiang: 0000-0003-0488-1987

Yongfeng Lu: 0000-0002-5942-1999

Notes

The authors declare no competing financial interest.

■ ACKNOWLEDGMENTS

This research was financially supported by the National Science Foundation (CMMI 1129613, CMMI 126512) and the Nebraska Center for Energy Science Research. Work by Z.X., J.S., and X.H. was supported by the U.S. Department of Energy (DOE), Office of Science, Basic Energy Sciences (BES), under Award No. DE-SC0016153 (scanning probe studies, device fabrication, and electrical characterizations). The research was performed in part in the Nebraska Nanoscale Facility: National Nanotechnology Coordinated Infrastructure, the Nanoengineering Research Core Facility.

■ REFERENCES

(1) Mak, K. F.; Lee, C.; Hone, J.; Shan, J.; Heinz, T. F. Atomically thin MoS_2: a new direct-gap semiconductor. *Phys. Rev. Lett.* **2010**, *105*, 136805.

(2) Splendiani, A.; Sun, L.; Zhang, Y.; Li, T.; Kim, J.; Chim, C.-Y.; Galli, G.; Wang, F. Emerging photoluminescence in monolayer MoS_2. *Nano Lett.* **2010**, *10*, 1271−1275.

(3) Xiao, D.; Liu, G.-B.; Feng, W.; Xu, X.; Yao, W. Coupledspin and valley physics in monolayers of MoS_2 and other group-VI dichalcogenides. *Phys. Rev. Lett.* **2012**, *108*, 196802.

(4) Mak, K. F.; He, K.; Shan, J.; Heinz, T. F. Control of valley polarization in monolayer MoS_2 by optical helicity. *Nat. Nanotechnol.* **2012**, *7*, 494−498.

(5) Cao, T.; Wang, G.; Han, W.; Ye, H.; Zhu, C.; Shi, J.; Niu, Q.; Tan, P.; Wang, E.; Liu, B.; et al. Valley-selective circular dichroism of monolayer molybdenum disulphide. *Nat. Commun.* **2012**, *3*, 887.

(6) Li, Y.; Rao, Y.; Mak, K. F.; You, Y.; Wang, S.; Dean, C. R.; Heinz, T. F. Probing symmetry properties of few-layer MoS_2 and h-BN by optical second-harmonic generation. *Nano Lett.* **2013**, *13*, 3329−3333.

(7) Kumar, N.; Najmaei, S.; Cui, Q.; Ceballos, F.; Ajayan, P. M.; Lou, J.; Zhao, H. Second harmonic microscopy of monolayer MoS_2. *Phys. Rev. B: Condens. Matter Mater. Phys.* **2013**, *87*, 161403.

(8) Malard, L. M.; Alencar, T. V.; Barboza, A. P. M.; Mak, K. F.; de Paula, A. M. Observation of Intense Second Harmonic Generation From MoS_2 Atomic Crystals. *Phys. Rev. B: Condens. Matter Mater. Phys.* **2013**, *87*, 201401.

(9) Li, D.; Xiong, W.; Jiang, L.; Xiao, Z.; Rabiee Golgir, H.; Wang, M.; Huang, X.; Zhou, Y.; Lin, Z.; Song, J.; et al. Multimodal nonlinear optical imaging of MoS_2 and MoS_2-based van der Waals heterostructures. *ACS Nano* **2016**, *10*, 3766−3775.

(10) Radisavljevic, B.; Radenovic, A.; Brivio, J.; Giacometti, V.; Kis, A. Single-layer MoS_2 transistors. *Nat. Nanotechnol.* **2011**, *6*, 147−150.

(11) Podzorov, V.; Gershenson, M.; Kloc, C.; Zeis, R.; Bucher, E. High-mobility field-effect transistors based on transition metal dichalcogenides. *Appl. Phys. Lett.* **2004**, *84*, 3301−3303.

(12) Novoselov, K.; Jiang, D.; Schedin, F.; Booth, T.; Khotkevich, V.; Morozov, S.; Geim, A. Two-dimensional atomic crystals. *Proc. Natl. Acad. Sci. U. S. A.* **2005**, *102*, 10451−10453.

(13) Radisavljevic, B.; Whitwick, M. B.; Kis, A. Integrated circuits and logic operations based on single-layer MoS_2. *ACS Nano* **2011**, *5*, 9934−9938.

(14) Wang, H.; Yu, L.; Lee, Y.-H.; Shi, Y.; Hsu, A.; Chin, M. L.; Li, L.-J.; Dubey, M.; Kong, J.; Palacios, T. Integrated circuits based on bilayer MoS_2 transistors. *Nano Lett.* **2012**, *12*, 4674−4680.

(15) Yin, Z.; Li, H.; Li, H.; Jiang, L.; Shi, Y.; Sun, Y.; Lu, G.; Zhang, Q.; Chen, X.; Zhang, H. Single-layer MoS_2 phototransistors. *ACS Nano* **2012**, *6*, 74−80.

(16) Lopez-Sanchez, O.; Lembke, D.; Kayci, M.; Radenovic, A.; Kis, A. Ultrasensitive photodetectors based on monolayer MoS_2. *Nat. Nanotechnol.* **2013**, *8*, 497−501.

(17) Tsai, M.-L.; Su, S.-H.; Chang, J.-K.; Tsai, D.-S.; Chen, C.-H.; Wu, C.-I.; Li, L.-J.; Chen, L.-J.; He, J.-H. Monolayer MoS_2 heterojunction solar cells. *ACS Nano* **2014**, *8*, 8317−8322.

(18) He, Q.; Zeng, Z.; Yin, Z.; Li, H.; Wu, S.; Huang, X.; Zhang, H. Fabrication of flexible MoS_2 thin-film transistor arrays for practical gas-sensing applications. *Small* **2012**, *8*, 2994−2999.

(19) Li, H.; Yin, Z.; He, Q.; Li, H.; Huang, X.; Lu, G.; Fam, D. W. H.; Tok, A. I. Y.; Zhang, Q.; Zhang, H. Fabrication of single-and multilayer MoS_2 film-based field-effect transistors for sensing NO at room temperature. *Small* **2012**, *8*, 63−67.

DOI: 10.1021/acs.nanolett.7b05473
Nano Lett. 2018, 18, 2021−2032

(20) Wang, S.; Yu, H.; Zhang, H.; Wang, A.; Zhao, M.; Chen, Y.; Mei, L.; Wang, J. Broadband few-layer MoS_2 saturable absorbers. *Adv. Mater.* **2014**, *26*, 3538−3544.
(21) Mao, D.; Wang, Y.; Ma, C.; Han, L.; Jiang, B.; Gan, X.; Hua, S.; Zhang, W.; Mei, T.; Zhao, J. WS_2 mode-locked ultrafast fiber laser. *Sci. Rep.* **2015**, *5*, 7965.
(22) Ye, Z.; Sun, D.; Heinz, T. F. Optical manipulation of valley pseudospin. *Nat. Phys.* **2016**, *13*, 26−29.
(23) Sangwan, V. K.; Jariwala, D.; Kim, I. S.; Chen, K.-S.; Marks, T. J.; Lauhon, L. J.; Hersam, M. C. Gate-tunable memristive phenomena mediated by grain boundaries in single-layer MoS_2. *Nat. Nanotechnol.* **2015**, *10*, 403−406.
(24) Cheng, P.; Sun, K.; Hu, Y. H. Memristive behavior and ideal memristor of 1T phase MoS_2 nanosheets. *Nano Lett.* **2016**, *16*, 572−576.
(25) Voiry, D.; Mohite, A.; Chhowalla, M. Phase engineering of transition metal dichalcogenides. *Chem. Soc. Rev.* **2015**, *44*, 2702−2712.
(26) Kappera, R.; Voiry, D.; Yalcin, S. E.; Branch, B.; Gupta, G.; Mohite, A. D.; Chhowalla, M. Phase-engineered low-resistance contacts for ultrathin MoS_2 transistors. *Nat. Mater.* **2014**, *13*, 1128−1134.
(27) Acerce, M.; Voiry, D.; Chhowalla, M. Metallic 1T phase MoS_2 nanosheets as supercapacitor electrode materials. *Nat. Nanotechnol.* **2015**, *10*, 313−318.
(28) Voiry, D.; Goswami, A.; Kappera, R.; e Silva, C. d. C. C.; Kaplan, D.; Fujita, T.; Chen, M.; Asefa, T.; Chhowalla, M. Covalent functionalization of monolayered transition metal dichalcogenides by phase engineering. *Nat. Chem.* **2015**, *7*, 45−49.
(29) Chang, K.; Hai, X.; Pang, H.; Zhang, H.; Shi, L.; Liu, G.; Liu, H.; Zhao, G.; Li, M.; Ye, J. Targeted synthesis of 2H-and 1T-phase MoS_2 monolayers for catalytic hydrogen evolution. *Adv. Mater.* **2016**, *28*, 10033−10041.
(30) Cho, S.; Kim, S.; Kim, J. H.; Zhao, J.; Seok, J.; Keum, D. H.; Baik, J.; Choe, D.-H.; Chang, K.; Suenaga, K.; et al. Phase patterning for ohmic homojunction contact in $MoTe_2$. *Science* **2015**, *349*, 625−628.
(31) Wang, Y.; Xiao, J.; Zhu, H.; Li, Y.; Alsaid, Y.; Fong, K. Y.; Zhou, Y.; Wang, S.; Shi, W.; Wang, Y.; et al. Structural phase transition in monolayer $MoTe_2$ driven by electrostatic doping. *Nature* **2017**, *550*, 487−491.
(32) Howell, S. L.; Jariwala, D.; Wu, C.-C.; Chen, K.-S.; Sangwan, V. K.; Kang, J.; Marks, T. J.; Hersam, M. C.; Lauhon, L. J. Investigation of band-offsets at monolayer−multilayer MoS_2 junctions by scanning photocurrent microscopy. *Nano Lett.* **2015**, *15*, 2278−2284.
(33) Li, M.-Y.; Chen, C.-H.; Shi, Y.; Li, L.-J. Heterostructures based on two-dimensional layered materials and their potential applications. *Mater. Today* **2016**, *19*, 322−335.
(34) Jariwala, D.; Marks, T. J.; Hersam, M. C. Mixed-dimensional van der Waals heterostructures. *Nat. Mater.* **2017**, *16*, 170−181.
(35) Wang, H.; Liu, F.; Fu, W.; Fang, Z.; Zhou, W.; Liu, Z. Two-dimensional heterostructures: fabrication, characterization, and application. *Nanoscale* **2014**, *6*, 12250−12272.
(36) Zhang, X.; Liao, Q.; Liu, S.; Kang, Z.; Zhang, Z.; Du, J.; Li, F.; Zhang, S.; Xiao, J.; Liu, B.; et al. Poly (4-styrenesulfonate)-induced sulfur vacancy self-healing strategy for monolayer MoS_2 homojunction photodiode. *Nat. Commun.* **2017**, *8*, 15881.
(37) Xiao, Z.; Song, J.; Ferry, D. K.; Ducharme, S.; Hong, X. Ferroelectric-domain-patterning-controlled schottky junction state in Monolayer MoS_2. *Phys. Rev. Lett.* **2017**, *118*, 236801.
(38) Wang, Q. H.; Kalantar-Zadeh, K.; Kis, A.; Coleman, J. N.; Strano, M. S. Electronics and optoelectronics of two-dimensional transition metal dichalcogenides. *Nat. Nanotechnol.* **2012**, *7*, 699−712.
(39) Wong, S. L.; Liu, H.; Chi, D. Recent progress in chemical vapor deposition growth of two-dimensional transition metal dichalcogenides. *Prog. Cryst. Growth Charact. Mater.* **2016**, *62*, 9−28.
(40) Li, D.; Zou, Q.; Rabiee-Golgir, H.; Keramatnejad, K.; Huang, X.; Song, J.; Xiao, Z.; Fan, L.; Hong, X.; Jiang, L.; et al. Controlled defect creation and removal in graphene and MoS_2 monolayers. *Nanoscale* **2017**, *9*, 8997−9008.
(41) Lee, Y. H.; Zhang, X. Q.; Zhang, W.; Chang, M. T.; Lin, C. T.; Chang, K. D.; Yu, Y. C.; Wang, J. T. W.; Chang, C. S.; Li, L. J.; et al. Synthesis of large-area MoS_2 atomic layers with chemical vapor deposition. *Adv. Mater.* **2012**, *24*, 2320−2325.
(42) Chen, J.; Tang, W.; Tian, B.; Liu, B.; Zhao, X.; Liu, Y.; Ren, T.; Liu, W.; Geng, D.; Jeong, H. Y.; et al. Chemical vapor deposition of high-quality large-sized MoS2 crystals on silicon dioxide substrates. *Adv. Sci.* **2016**, *3*, 1500033.
(43) Kang, K.; Xie, S.; Huang, L.; Han, Y.; Huang, P. Y.; Mak, K. F.; Kim, C.-J.; Muller, D.; Park, J. High-mobility three-atom-thick semiconducting films with wafer-scale homogeneity. *Nature* **2015**, *520*, 656−660.
(44) Najmaei, S.; Liu, Z.; Zhou, W.; Zou, X.; Shi, G.; Lei, S.; Yakobson, B. I.; Idrobo, J.-C.; Ajayan, P. M.; Lou, J. Vapour phase growth and grain boundary structure of molybdenum disulphide atomic layers. *Nat. Mater.* **2013**, *12*, 754−759.
(45) Van Der Zande, A. M.; Huang, P. Y.; Chenet, D. A.; Berkelbach, T. C.; You, Y.; Lee, G.-H.; Heinz, T. F.; Reichman, D. R.; Muller, D. A.; Hone, J. C. Grains and grain boundaries in highly crystalline monolayer molybdenum disulphide. *Nat. Mater.* **2013**, *12*, 554−561.
(46) Li, J.; Hu, C.; Wu, H.; Liu, Z.; Cheng, S.; Zhang, W.; Shu, H.; Chang, H. Facile preparation of single MoS_2 atomic crystals with highly tunable photoluminescence by morphology and atomic structure. *Cryst. Growth Des.* **2016**, *16*, 7094−7101.
(47) Bilgin, I.; Liu, F.; Vargas, A.; Winchester, A.; Man, M. K.; Upmanyu, M.; Dani, K. M.; Gupta, G.; Talapatra, S.; Mohite, A. D.; et al. Chemical vapor deposition synthesized atomically thin molybdenum disulfide with optoelectronic-grade crystalline quality. *ACS Nano* **2015**, *9*, 8822−8832.
(48) Lince, J. R.; Hilton, M. R.; Bommannavar, A. S. Oxygen substitution in sputter-deposited MoS_2 films studied by extended X-ray absorption fine structure, X-ray photoelectron spectroscopy and X-ray diffraction. *Surf. Coat. Technol.* **1990**, *43-44*, 640−651.
(49) Ionescu, R.; George, A.; Ruiz, I.; Favors, Z.; Mutlu, Z.; Liu, C.; Ahmed, K.; Wu, R.; Jeong, J. S.; Zavala, L.; et al. Oxygen etching of thick MoS_2 films. *Chem. Commun.* **2014**, *50*, 11226−11229.
(50) Lin, Y.-C.; Zhang, W.; Huang, J.-K.; Liu, K.-K.; Lee, Y.-H.; Liang, C.-T.; Chu, C.-W.; Li, L.-J. Wafer-scale MoS_2 thin layers prepared by MoO_3 sulfurization. *Nanoscale* **2012**, *4*, 6637−6641.
(51) Zhan, Y.; Liu, Z.; Najmaei, S.; Ajayan, P. M.; Lou, J. Large-area vapor-phase growth and characterization of MoS_2 atomic layers on a SiO_2 substrate. *Small* **2012**, *8*, 966−971.
(52) Tai, G.; Zeng, T.; Yu, J.; Zhou, J.; You, Y.; Wang, X.; Wu, H.; Sun, X.; Hu, T.; Guo, W. Fast and large-area growth of uniform MoS_2 monolayers on molybdenum foils. *Nanoscale* **2016**, *8*, 2234−2241.
(53) Robertson, J.; Liu, X.; Yue, C.; Escarra, M.; Wei, J. Wafer-scale synthesis of monolayer and few-layer MoS_2 via thermal vapor sulfurization. *2D Mater.* **2017**, *4*, 045007.
(54) Chen, C.-C.; Kuo, C.-J.; Liao, C.-D.; Chang, C.-F.; Tseng, C.-A.; Liu, C.-R.; Chen, Y.-T. Growth of large-area graphene single crystals in confined reaction space with diffusion-driven chemical vapor deposition. *Chem. Mater.* **2015**, *27*, 6249−6258.
(55) Yu, Y.; Li, C.; Liu, Y.; Su, L.; Zhang, Y.; Cao, L. Controlled scalable synthesis of uniform, high-quality monolayer and few-layer MoS_2 films. *Sci. Rep.* **2013**, *3*, 1866.
(56) Li, B.; Gong, Y.; Hu, Z.; Brunetto, G.; Yang, Y.; Ye, G.; Zhang, Z.; Lei, S.; Jin, Z.; Bianco, E.; et al. Solid−vapor reaction growth of transition-metal dichalcogenide monolayers. *Angew. Chem.* **2016**, *128*, 10814−10819.
(57) Fan, X.; Xu, P.; Zhou, D.; Sun, Y.; Li, Y. C.; Nguyen, M. A. T.; Terrones, M.; Mallouk, T. E. Fast and efficient preparation of exfoliated 2H MoS_2 nanosheets by sonication-assisted lithium intercalation and infrared laser-induced 1T to 2H phase reversion. *Nano Lett.* **2015**, *15*, 5956−5960.
(58) Kang, Y.; Najmaei, S.; Liu, Z.; Bao, Y.; Wang, Y.; Zhu, X.; Halas, N. J.; Nordlander, P.; Ajayan, P. M.; Lou, J.; et al. Plasmonic

DOI: 10.1021/acs.nanolett.7b05473
Nano Lett. 2018, 18, 2021−2032

hot electron induced structural phase transition in a MoS_2 monolayer. *Adv. Mater.* **2014**, *26*, 6467−6471.
(59) Eda, G.; Yamaguchi, H.; Voiry, D.; Fujita, T.; Chen, M.; Chhowalla, M. Photoluminescence from chemically exfoliated MoS_2. *Nano Lett.* **2011**, *11*, 5111−5116.
(60) Lin, Y.-C.; Dumcenco, D. O.; Huang, Y.-S.; Suenaga, K. Atomic mechanism of the semiconducting-to-metallic phase transition in single-layered MoS2. *Nat. Nanotechnol.* **2014**, *9*, 391−396.
(61) Li, Y.; Huang, L.; Li, B.; Wang, X.; Zhou, Z.; Li, J.; Wei, Z. Co-nucleus 1D/2D heterostructures with Bi_2S_3 nanowire and MoS_2 monolayer: One-step growth and defect-induced formation mechanism. *ACS Nano* **2016**, *10*, 8938−8946.
(62) Liu, Y.; Nan, H.; Wu, X.; Pan, W.; Wang, W.; Bai, J.; Zhao, W.; Sun, L.; Wang, X.; Ni, Z. Layer-by-layer thinning of MoS_2 by plasma. *ACS Nano* **2013**, *7*, 4202−4209.
(63) Cain, J. D.; Shi, F.; Wu, J.; Dravid, V. P. Growth mechanism of transition metal dichalcogenide monolayers: the role of self-seeding fullerene nuclei. *ACS Nano* **2016**, *10*, 5440−5445.
(64) Ochedowski, O.; Marinov, K.; Scheuschner, N.; Poloczek, A.; Bussmann, B. K.; Maultzsch, J.; Schleberger, M. Effect of contaminations and surface preparation on the work function of single layer MoS_2. *Beilstein J. Nanotechnol.* **2014**, *5*, 291.
(65) Han, G. H.; Kybert, N. J.; Naylor, C. H.; Lee, B. S.; Ping, J.; Park, J. H.; Kang, J.; Lee, S. Y.; Lee, Y. H.; Agarwal, R.; et al. Seeded growth of highly crystalline molybdenum disulphide monolayers at controlled locations. *Nat. Commun.* **2015**, *6*, 6128.
(66) Kim, I. S.; Sangwan, V. K.; Jariwala, D.; Wood, J. D.; Park, S.; Chen, K.-S.; Shi, F.; Ruiz-Zepeda, F.; Ponce, A.; Jose-Yacaman, M. Influence of stoichiometry on the optical and electrical properties of chemical vapor deposition derived MoS_2. *ACS Nano* **2014**, *8*, 10551−10558.
(67) Yin, X.; Ye, Z.; Chenet, D. A.; Ye, Y.; O'Brien, K.; Hone, J. C.; Zhang, X. Edge nonlinear optics on a MoS_2 atomic monolayer. *Science* **2014**, *344*, 488−490.
(68) Hsu, W.-T.; Zhao, Z.-A.; Li, L.-J.; Chen, C.-H.; Chiu, M.-H.; Chang, P.-S.; Chou, Y.-C.; Chang, W.-H. Second harmonic generation from artificially stacked transition metal dichalcogenide twisted bilayers. *ACS Nano* **2014**, *8*, 2951−2958.
(69) Cheng, J.; Jiang, T.; Ji, Q.; Zhang, Y.; Li, Z.; Shan, Y.; Zhang, Y.; Gong, X.; Liu, W.; Wu, S. Kinetic nature of grain boundary formation in as-grown MoS_2 monolayers. *Adv. Mater.* **2015**, *27*, 4069−4074.
(70) Kunc, J.; Hu, Y.; Palmer, J.; Guo, Z.; Hankinson, J.; Gamal, S. H.; Berger, C.; De Heer, W. A. Planar edge Schottky barrier-tunneling transistors using epitaxial graphene/SiC junctions. *Nano Lett.* **2014**, *14*, 5170−5175.
(71) Li, H.-M.; Lee, D.; Qu, D.; Liu, X.; Ryu, J.; Seabaugh, A.; Yoo, W. J. Ultimate thin vertical p−n junction composed of two-dimensional layered molybdenum disulfide. *Nat. Commun.* **2015**, *6*, 6564.
(72) Park, W.; Baik, J.; Kim, T.-Y.; Cho, K.; Hong, W.-K.; Shin, H.-J.; Lee, T. Photoelectron spectroscopic imaging and device applications of large-area patternable single-layer MoS_2 synthesized by chemical vapor deposition. *ACS Nano* **2014**, *8*, 4961−4968.
(73) Lee, J.; Pak, S.; Giraud, P.; Lee, Y. W.; Cho, Y.; Hong, J.; Jang, A.; Chung, H. S.; Hong, W. K.; Jeong, H. Y.; et al. Thermodynamically stable synthesis of large-scale and highly crystalline transition metal dichalcogenide monolayers and their unipolar n−n heterojunction devices. *Adv. Mater.* **2017**, *29*, 1702206.
(74) Song, J.; Lu, H.; Foreman, K.; Li, S.; Tan, L.; Adenwalla, S.; Gruverman, A.; Ducharme, S. Ferroelectric polymer nanopillar arrays on flexible substrates by reverse nanoimprint lithography. *J. Mater. Chem. C* **2016**, *4*, 5914−5921.
(75) Nalwa, H. S. *Ferroelectric and dielectric thin films*; Academic Press, 2001.
(76) Song, J.; Lu, H.; Gruverman, A.; Ducharme, S. Polarization imaging in ferroelectric polymer thin film capacitors by pyroelectric scanning microscopy. *Appl. Phys. Lett.* **2014**, *104*, 192901.
(77) Li, D.; Zhou, Y. S.; Huang, X.; Jiang, L.; Silvain, J.-F.; Lu, Y. F. In situ imaging and control of layer-by-layer femtosecond laser thinning of graphene. *Nanoscale* **2015**, *7*, 3651−3659.
(78) Blöchl, P. E. Projector augmented-wave method. *Phys. Rev. B: Condens. Matter Mater. Phys.* **1994**, *50*, 17953.
(79) Kresse, G.; Furthmüller, J. Efficient iterative schemes for ab initio total-energy calculations using a plane-wave basis set. *Phys. Rev. B: Condens. Matter Mater. Phys.* **1996**, *54*, 11169.
(80) Monkhorst, H. J.; Pack, J. D. Special points for Brillouin-zone integrations. *Phys. Rev. B* **1976**, *13*, 5188.
(81) Le, D.; Rawal, T. B.; Rahman, T. S. Single-layer MoS_2 with sulfur vacancies: structure and catalytic application. *J. Phys. Chem. C* **2014**, *118*, 5346−5351.

DOI: 10.1021/acs.nanolett.7b05473
Nano Lett. 2018, 18, 2021−2032

View publication stats